The International Journal of Advanced Manufacturing Technology (2022) 120:1695–1706
https://doi.org/10.1007/s00170-022-08894-x

ORIGINAL ARTICLE

On the grinding performance of alumina wheels in ultrasonic vibration–assisted grinding of hardened GCr15 steel

Yutong Qiu[1] · Biao Zhao[1] · Yang Cao[1] · Wenfeng Ding[1] · Yucan Fu[1] · Changlan Pu[2]

Received: 26 November 2021 / Accepted: 7 February 2022 / Published online: 14 February 2022

Abstract

Composite manufacturing with multiple energy fields is an important source of processing technology innovation. In this work, comparative experiments on the conventional grinding and ultrasonic vibration–assisted grinding (UVAG) of hardened GCr15 steel were conducted with white alumina (WA) wheel. The grinding wheel wear patterns and chips were characterised. In addition, grinding force, force ratio and ground surface quality were investigated to evaluate wheel performance. Results illustrate that the interaction between abrasive grains and workpiece in UVAG has the characteristics of high frequency and discontinuity. The wear property of abrasive grains is changed, and the grinding force is decreased because the generation of microfracture in abrasive grains improves the self-sharpening of the grinding wheel. Good surface quality is obtained. The surface roughness is reduced by up to 18.96%, and the number of defects on the machined surface is reduced through the superior reciprocating ironing of UVAG. Accordingly, WA wheel performance is improved by UVAG.

Keywords Wear behaviour · WA wheel · Hardened GCr15 steel · Ultrasonic vibration-assisted grinding

1 Introduction

In recent years, the demands of mechanical transmission systems have increased to meet the high performance requirements (e.g. thrust-to-weight ratio, reliability and service life) in modern aerospace, ship and automobile industry sectors. Gears are the key components of the abovementioned transmission systems; hence, their surface quality plays a crucial influence on the service performance of the whole system [1–4]. At present, the grinding process is usually applied as the final procedure to raise the dimension accuracy and surface integrity of gears [5, 6]. However, gear steels, such as GCr15 steels, exhibit high hardness (reaching HRC 58–62), high tensile strength and low thermal conductivity after the carburising and quenching process; these characteristics are typical to difficult-to-cut materials [7–9]. In this case, severe tool wear and poor ground surface quality are inevitable because of the lack of sufficient coolant in the grinding arc zone during the conventional grinding (CG) process [10, 11]. Thus, improving the wear resistance of alumina wheels and coolant conditions inside the grinding arc zone is crucial in achieving desirable grinding performance and good machining quality.

Complex machining technology of ultrasonic vibration–assisted grinding (UVAG) has been the major approach for process improvement, and this multienergy field composite manufacturing is an important source of machining technology innovation [12–14]. Ultrasonic vibration forms different material removal mechanisms for grinding different engineering materials; these mechanisms can achieve ductility domain grinding of brittle materials or change the properties and state of plastic materials through acoustic softening [15, 16]. Consequently, this complex machining technology is usually used to improve the machining efficiency and surface integrity of difficult-to-cut materials at home and abroad. Bhaduri et al. [17, 18] conducted a comparison experiment to evaluate the ground surface roughness of TiAl intermetallic and Inconel 718 superalloy under CG and UVAG processes. They found that the grinding quality can be considerably improved because of the trajectory interference between abrasive grains by applying the ultrasonic vibration method. Yu et al. [19] indicated that the polishing quality of Inconel 718 can be improved considerably

✉ Biao Zhao
zhaobiao@nuaa.edu.cn

[1] National Key Laboratory of Science and Technology On Helicopter Transmission, Nanjing University of Aeronautics and Astronautics, Nanjing 210016, China

[2] Avic Cheng'du Aircraft Industrial (Group) Co. LTD, Chengdu 610092, China

Table 1 Chemical composition of GCr15

Element	C	Si	Mn	P	S	Cr	Ni	Mo	Fe
Component/%	1.03	0.227	0.353	0.007	0.003	1.46	0.015	0.0096	Bal

under the changed motion state of the free abrasive particles because of ultrasonic vibration. Nik et al. [20] proved that applying UVAG also contributed to reducing grinding forces and improving the surface quality of Ti-6Al-4 V alloy grinding. In addition, Wang et al. [21] performed numerical simulation analysis on the surface generation process in UVAG. The crossing and superposition of adjacent abrasive trajectories are promoted by the increase in amplitude. Thus, the surface roughness is reduced. Furthermore, the cutting edges of abrasive grains tend to produce the macrofracture and pull-out under the traditional grinding process, leading to poor ground surface quality [22–24]. However, the influences of ultrasonic vibration on the material removal mechanism of grinding hardened steel and tool wear property were seldom analysed.

The tool wear behaviour in the traditional grinding of difficult-to-cut materials has been investigated in many works to improve the ground surface quality by controlling the tool wear. For example, Li et al. [25] analysed the grain wear evolution through acoustic emission testing. The results showed that abrasive wear is divided into three stages, and the wear state is gradually increasing. Xi et al. [26] compared and evaluated tool wear characteristics during grinding Ti_2AlNb, Ti-6Al-4 V and Inconel 718. The most severe tool wear can be observed in the grinding of Ti_2AlNb intermetallic because of the strong affinity with SiC abrasives. Madopothula et al. [27] studied the grinding of AISI 52100 with two kinds of corundum grinding wheels. The results proved that sol–gel abrasive grains are rubbed, causing the main material to change from shearing to plough and friction. The abrasive fracture occurred when the white alumina (WA) wheel was grinding. Yang et al. [28] researched the form grinding of a 20CrMnTi steel tooth with a self-developed microcrystalline corundum wheel. The excellent self-sharpening of microcrystalline corundum abrasive increases the number of effective abrasive grains and reduced the extrusion and friction between the chip and the workpiece. In addition to improving ordinary abrasive grinding wheel, applying a multienergy field processing method is also a way to reduce grinding wheel wear and improve grinding performance. Currently, the grinding wheel wear properties in UVAG for the controllability of UVAG process are still being explored.

Thus, the present study conducts a comparative investigation on CG and UVAG to explore the effect of grinding parameters on wear evaluation and grinding performance for the development of the UVAG strategy of hardened gear steel surfaces. Section 2 describes the experimental conditions and steps of UVAG of hardened GCr15 steel with WA wheel. Sections 3 and 4 indicate the analysis and conclusions, respectively.

2 Materials and methods

2.1 Experimental procedures and materials

The workpiece material used in this study is GCr15 hardened steel, and its chemical composition content and mechanical properties are listed in Tables 1 and 2. The workpiece was prepared by wire-electrode cutting techniques with the dimension of 30 mm in length, 10 mm in width and 12 mm in height. Then, the top surface of the workpiece was firstly machined to the surface roughness of 0.8 μm before the grinding experiments. The hardness distribution of the surface/subsurface layer of the workpiece before the experiment is shown in Fig. 1. Given the good hardenability of GCr15 steel, the hardness of the material can reach HRC 60–65 within a depth of 2 mm from the surface.

A precision surface grinding machine (BLOHM Profimat MT-408) coupled with coolant systems was used to perform the grinding experiments, as shown in Fig. 2a. The self-developed ultrasonic vibration system (Fig. 2b) was fixed to the workbench with support legs. The ultrasonic generator outputs high-frequency electrical signals, which were converted into mechanical vibration by the connected transducer and magnified by the horn. In the end, the workpiece attached to a titanium alloy platform connected to the horn could vibrate. In addition, the grinding environment was very complex, and the workpiece was covered by the coolant in the grinding process. Thus, the dynamic amplitude signal in the grinding process could not be collected. Therefore, the amplitude value without grinding thermal load was adopted in this study. As shown in Fig. 2c, the grinding wheel is a WA wheel, which is suitable for grinding hardened steel. The model of the grinding wheel is

Table 2 Mechanical properties of GCr15

Yield strength $\sigma_{0.2}$ (MPa)	Tensile strength σ_b (MPa)	Elastic modulus (GPa)	Density ρ (g/cm^3)	Thermal conductivity k (W/m·K)	Rockwell hardness (HRC)
1394	1748	210	7.81	46.6	60

WA80F6V45M. The abrasive grain size of the grinding wheels is approximately 160–200 μm. The diameter of the grinding wheel d_s is 400 mm, and the axial width b_s is 20 mm. After each group of the grinding experiment, a single point diamond dresser was used to dress the grinding wheel. The dressing parameters were as follows: grinding speed of $v_c = 20$ m/s, workpiece speed rate of $f_c = 200$ mm/min and a total dressing depth of $a_H = 0.2$ mm. The detailed grinding process parameters are listed in Table 3. The material removal rate (MRR) Q'_w is expressed as Eq. (1): The material removal volume (MRV) of the first pass in reciprocating grinding $V_{r1} = l_w \cdot b_w \cdot a_p$. l_w and b_w is the length and width of the workpiece. A_p is the depth of cut. The cumulative removal of workpiece material volume in each group of experiments is $V_r = 450$ mm^3.

$$Q'_w = a_p \cdot v_w \tag{1}$$

The grinding force was collected by Kistler 9253B-type three-channel piezoelectric dynamometer, as shown in Fig. 2d. Then, it passed through the charge amplifier Kistler 5080A. Finally, it was measured on the software. The surface microstructure of the grinding wheel, chips and workpiece were characterised by a scanning electron microscope (Quanta 200 SEM), as shown in Fig. 2e. The machined surface roughness R_a was measured by Mahr M2 perthometer (cut length: 0.8 mm). The ground surface profile was obtained by Sensofar S Neox 3D confocal microscopy.

2.2 Tangential ultrasonic vibration method

In this work, tangential ultrasonic vibration was used for reciprocating surface grinding. The direction of the high-frequency vibration is parallel to the workpiece speed. The velocity of the grain in a cycle of reciprocating grinding can be presented as Eq. (2):

$$\begin{bmatrix} v_x \\ v_y \end{bmatrix} = \begin{bmatrix} (-1)^a \cdot v_w + v_s \cdot \cos \omega_s t + 2\pi f \cdot A\cos\left(2\pi f \cdot t + \varphi_0\right) \\ v_s \cdot \sin \omega_s t \end{bmatrix}, \begin{cases} a = 0, \text{down grinding} \\ a = 1, \text{up grinding} \end{cases}, \tag{2}$$

where v_s, v_w, f, A and t are the wheel speed, workpiece speed, ultrasonic frequency, ultrasonic amplitude and time, respectively; ω_s is the angular velocity of the abrasive wheel, $v_s = \omega_s \cdot d_s$, d_s is the wheel radius; and φ_0 denotes the initial phase of ultrasonic vibration. A single abrasive trajectory of CG and tangential UVAG in the grinding arc is shown in Fig. 3a.

This kind of grinding process has periodic reciprocating motion. The abrasive grain also has an intermittent effect with the workpiece on the micro view, as long as the grinding wheel and workpiece are separated on the macro

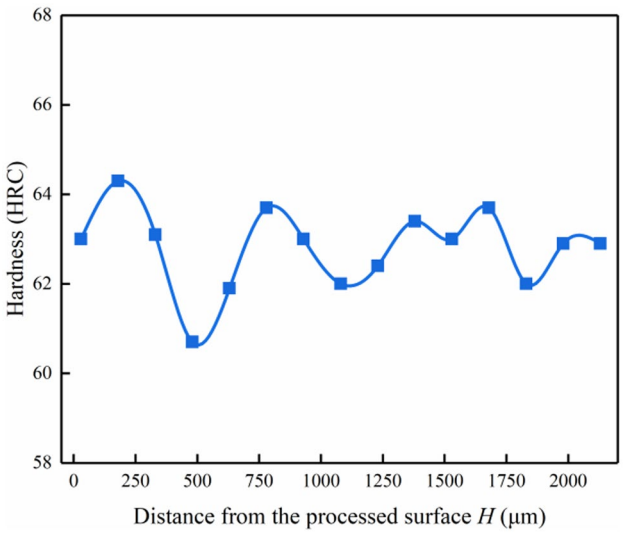

Fig. 1 Hardness distribution of the surface/subsurface layer of the workpiece before the experiment

view of the grinding process. According to reference [29], the separation condition of the grinding wheel and the workpiece can be expressed as follows:

$$v_w < 2\pi f \cdot A \tag{3}$$

Combine Eq. (1) and Eq. (3), the relationship between MRR and ultrasonic parameters can be expressed as follows:

$$Q'_w < 2\pi f \cdot A \cdot a_p \tag{4}$$

In the case of $(Q'_w)_{max} = 4.17$ mm^3/(mm·s), $(a_p)_{min} = 10$ μm and $f = 19.6$ kHz, $A = 6$ μm, intermittent effects exist under all parameter conditions in this study.

As shown in Fig. 3b, abrasive grain demonstrates the characteristic of separability during t_1–t_2. It could be seen that the vibrating speed was larger than the grain moving speed at the time of t_1 and the separating stage between abrasive grains and workpiece appeared. As the time reaches t_2, the vibrating speed becomes smaller than the grain moving speed, and thus this separating distance tended to a maximum value. With the time gone to t_3, this abrasive grain and workpiece start to contact again. A single whole contacting and separating process was then completed. The cutting time Δt between the abrasive and the workpiece can be described as

$$a_p = \frac{d_s}{2}(1 - \cos\varphi) = \frac{d_s}{2}\left(1 - \cos\left(\frac{2v_s}{d_s} \cdot \Delta t\right)\right), \tag{5}$$

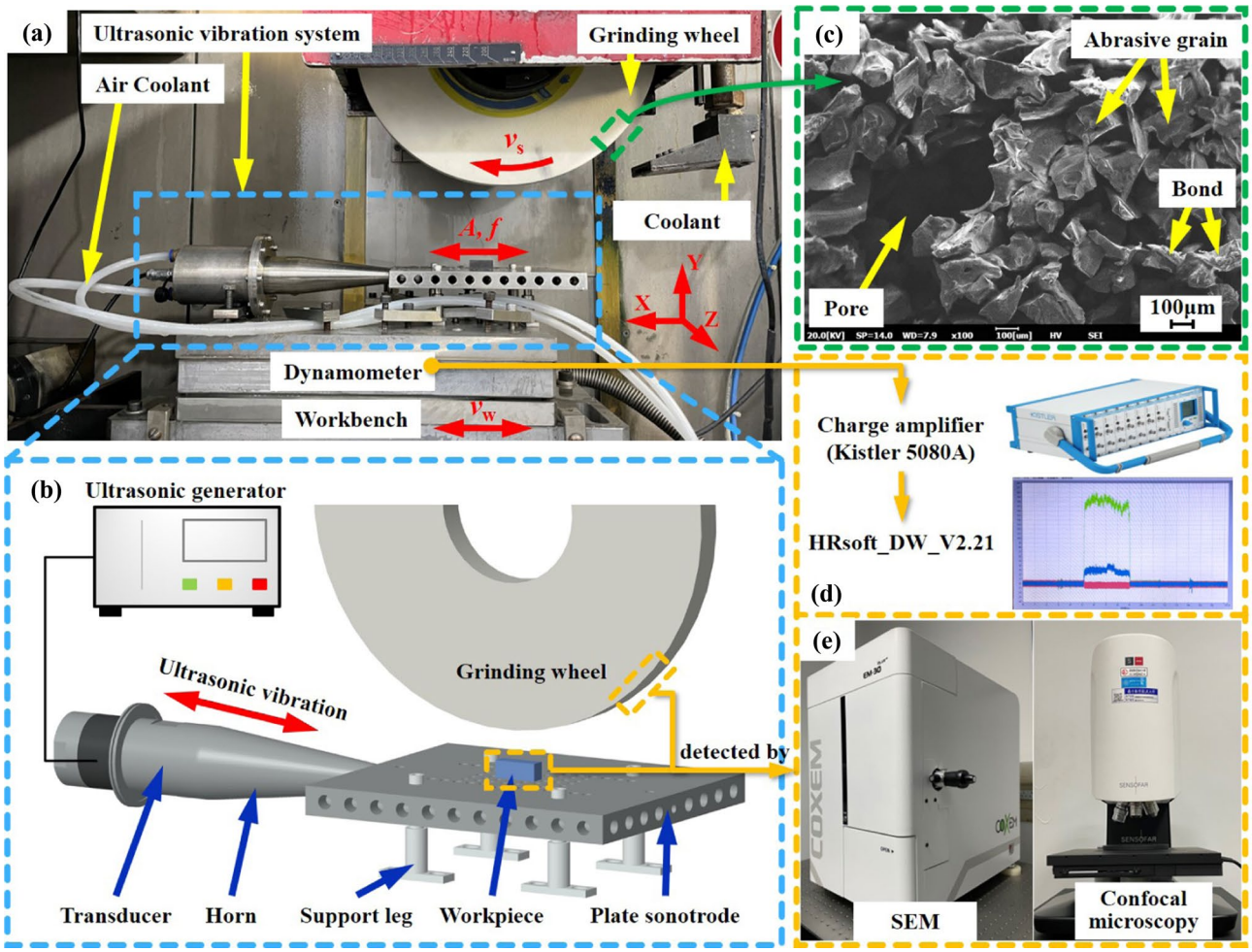

Fig. 2 Reciprocating surface grinding experimental setup (**a**), including ultrasonic vibration system (**b**), WA wheel (**c**), grinding force measuring system (**d**), and surface measuring device (**e**)

where $\frac{2v_s}{d_s} \cdot \Delta t$ is very small; thus, $cos\left(\frac{2v_s}{d_s} \cdot \Delta t\right) \approx 1 - \frac{1}{2}\left(\frac{2v_s}{d_s} \cdot \Delta t\right)^2$ and Δt can be expressed as

$$\Delta t = \frac{1}{v_s}\sqrt{a_p d_s}. \tag{6}$$

Under the condition of workpiece tangential ultrasonic vibration–assisted machining, the relative vibration number N between a single abrasive and the workpiece in the grinding arc can be expressed as

$$N = \frac{\Delta t}{T} = \frac{f}{v_s}\sqrt{a_p d_s}. \tag{7}$$

In the case of $a_p = 15$ μm, $d_s = 400$ mm, $v_s = 25$ m/s and $f = 19.6$ kHz, the abrasive grains vibrate for approximately two

Table 3 Grinding process parameters

Contents	Values
Machine tool	Blohm Profimat MT-408 surface grinder
Grinding mode	Reciprocating surface grinding
Abrasive wheel	WA wheel (mesh size of 80)
Ultrasonic frequency f (kHz)	19.6
Ultrasonic amplitude A (μm)	6
Wheel speed v_s (m/s)	25
Workpiece speed v_w (m/min)	Balance
Depth of cut a_p (μm)	10, 15, 20, 25
Material removal rate Q'_w (mm^3/(mm·s))	1.33, 1.5, 2, 2.67, 3.33, 4.17
Cooling condition	5% emulsified water, 90 L/min, pressure at 1.5 MPa

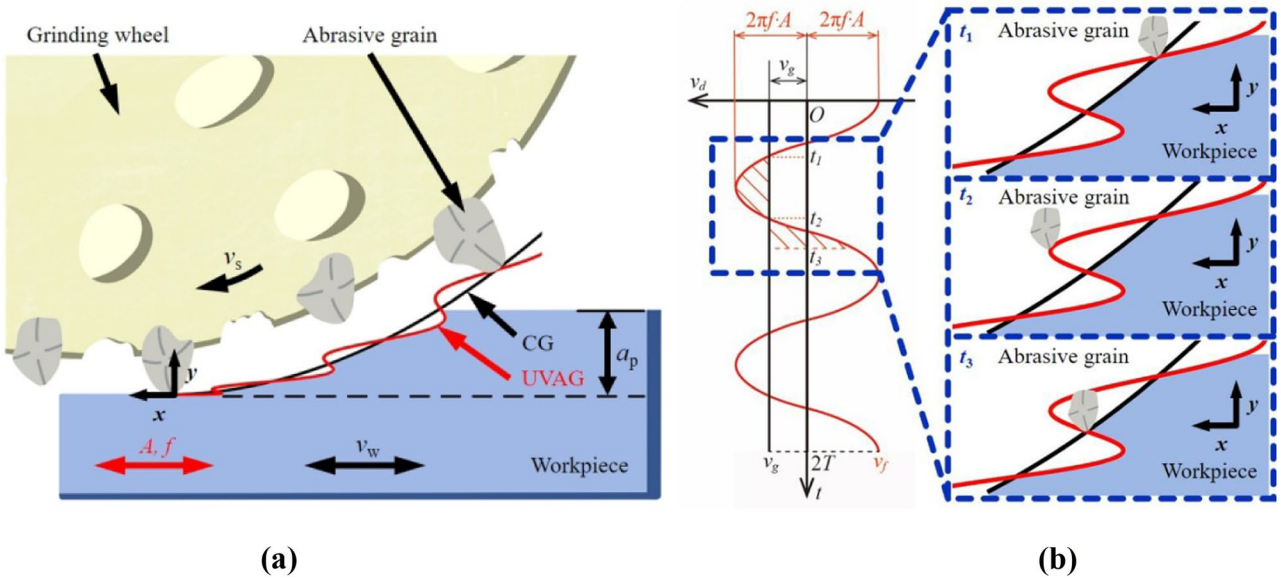

Fig. 3 Schematic of (**a**) abrasive trajectory of CG and tangential UVAG and (**b**) separation characteristics in UVAG process

cycles in the grinding arc, suggesting that the abrasive grains perform varying behaviour between the contact and separation of abrasive grain and workpiece in the grinding arc.

3 Results and discussion

3.1 Grinding force and force ratio

Grinding force is a crucial parameter to characterise the grinding process, and it has an important effect on tool wear and machined surface quality [30, 31]. The average value of three grinding force signals is selected as the grinding force value in this study to achieve reliable data. The graphs showing the grinding forces against MRR and MRV for the two grinding methods are detailed in Fig. 4.

As shown in Fig. 4a and b, the tangential grinding force F_t and the normal grinding force F_n of the two strategies exhibit a similar increasing trend with an increase in MRR. When the MRV of reciprocating grinding $V_r = 450$ mm^3 and the MRR increases from 1.33 mm^3/(mm·s) to 4.17 mm^3/(mm·s), the tangential grinding force of CG increases from 57.5 to 169.2 N. The normal grinding force also increases from 143.19 to 381.73 N. Moreover, the tangential force of UVAG increases from 52.12 to 144.42 N, and the normal force increases from 118.06 to 322.77 N. The grinding force under UVAG is smaller than that under CG. In UVAG, the maximum reductions in tangential force are 34.62%, 13.4% and 14.66% with V_{r1}, $V_r = 225$ mm^3 and $V_r = 450$ mm^3, respectively; the maximum reductions in normal force are 34.25%, 17.08% and 17.54% with V_{r1}, $V_r = 225$ mm^3 and $V_r = 450$ mm^3, respectively. The grinding force ratio F_n/F_t varies in the range of 2.06–2.49 and 2.02–2.32 with the increase in MRR in CG and UVAG, respectively (Fig. 4c). The WA wheel has an excellent grinding performance, and the grinding force ratio is small and stable because the grinding wheel has a good self-sharpening effect in UVAG. As shown in Fig. 4d, the tangential and normal grinding forces in CG increase from 74 to 87.17 N and from 162.52 to 179.71 N, respectively. The tangential and normal grinding forces in UVAG increase from 65.56 to 79.05 N and from 134.43 to 162.6 N, respectively. It could be included that when the MRR value varied in the range of 135–315 mm^3, the normal grinding force raised by 3.39%, from 141.65 to 146.45 N. However, as the MRR value increased to 180 mm^3, the normal grinding force reached 145.24 N, which is only 0.833% lower than that of 315 mm^3. In this case, the normal grinding force has a steady and constant stage at MRV of 180–315 mm^3 in UVAG. A different result is observed in CG, in which the normal grinding force keeps on increasing.

In UVAG, the material removal mechanism is changed because of the characteristic of separability. The cutting process is not continuous because of the high-frequency interaction between active abrasive grains and the workpiece surface. This process of multiple-impact interaction makes the material begin to roll over easily. Microcracks are formed in the grinding area, leading to effective material removal. Therefore, the grinding force is decreased [32]. Thus, the application of ultrasonic vibration improves the grinding performance of workpiece material. However, the increase in MRR results in large grinding loads [33], and the ultrasonic vibration effect on the grinding force reduction is reduced by the aggravated grinding wheel wear.

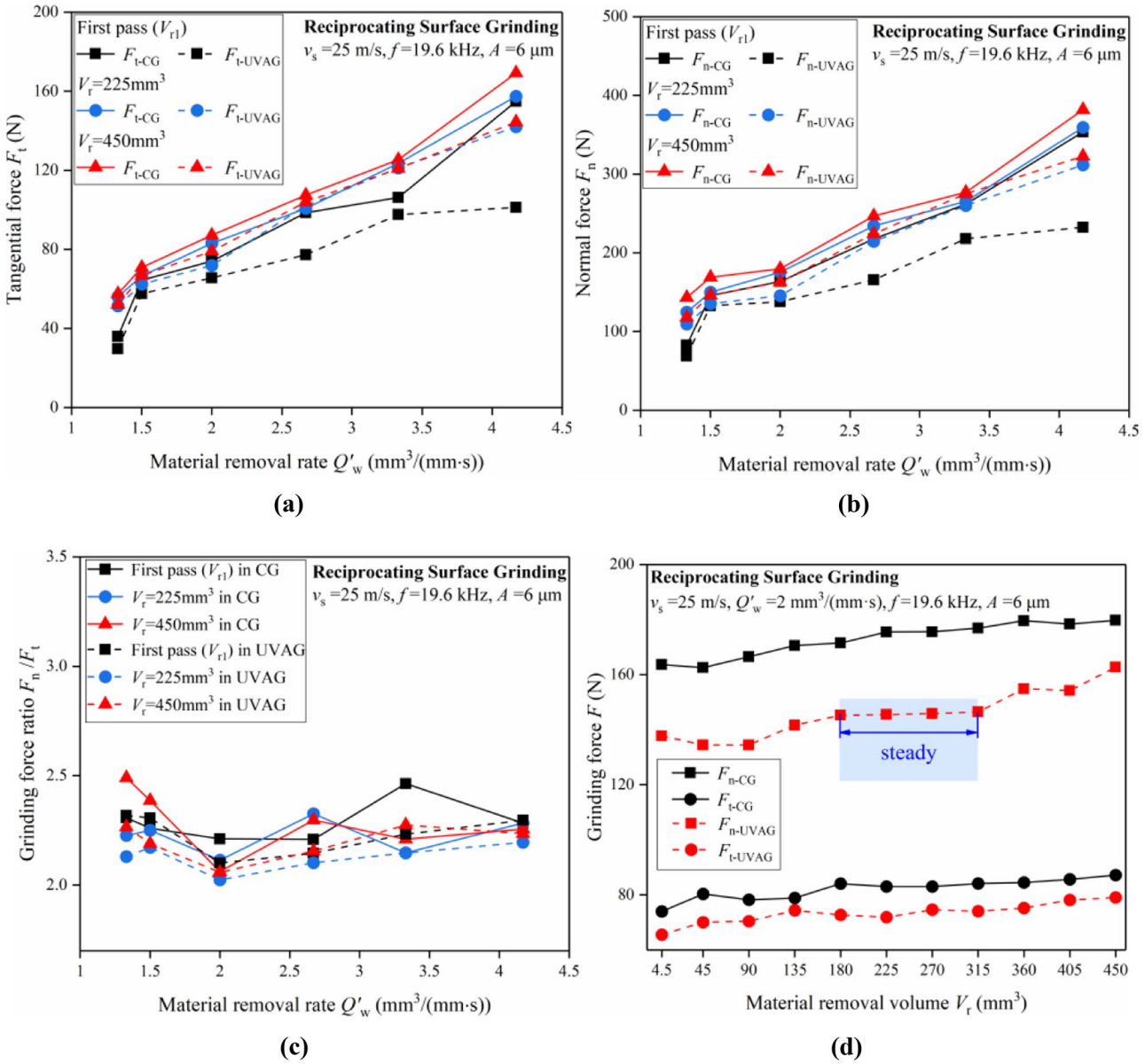

Fig. 4 Effects of MRR on the (**a**) tangential force, (**b**) normal force and (**c**) grinding force ratio for CG and UVAG and (**d**) grinding force versus MRV in CG and UVAG

3.2 Wear surface topography

The grains on the grinding wheel are subjected to heavy load during the grinding process, and the effective life of the grains is an important affecting factor in the performance of the grinding wheel. Figure 5 demonstrates the grinding wheel wear characteristics under the two grinding processes when grinding wheel speed $v_s = 25$ m/s and MRR = 2 mm^3/(mm·s). As shown in Fig. 5a-c, a mechanical clogging pore with abundant chips is obvious in area I under CG, and continuous chip adhesion can be observed on the surface of the abrasive grains in area II. In addition, the wear patterns of grain pull-out and wear-flat can be easily formed. Conversely, the open pore is relatively clean and conducive to heat dissipation under UVAG, as shown in areas I and II in Fig. 5d-f. The chip adhesion is reduced, and the wear morphology of the abrasive grains exhibits microfracture. In this case, multiple cutting edges are generated, and the self-sharpening capability of grinding wheels can be effectively increased by UVAG processes.

In the grinding process, the typical wear of the grinding wheel is friction wear, abrasive fragmentation and bond failure. Figure 6a illustrates the force and thermal loads of a single abrasive grain. The wear patterns of grains under

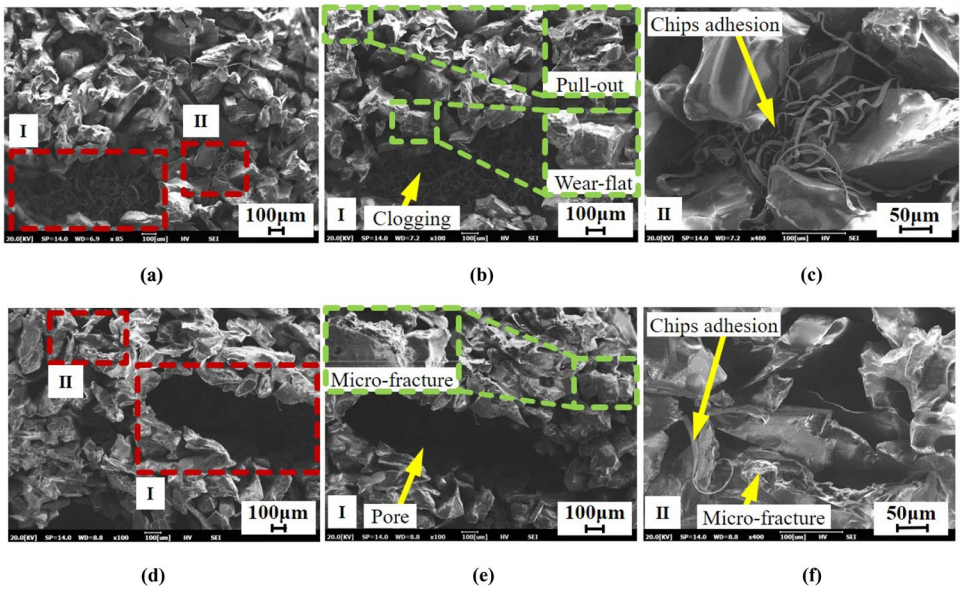

Fig. 5 SEM microstructures of wheel surface of grinding wheels under CG (**a**) and UVAG (**d**); (**b**), (**e**) magnified views of chip storage spaces and the characteristics of grain wear; (**c**), (**f**) magnified views of chip adhesion

heavy load can be divided into brittle fracture and plastic wear. Grain wear behaviours of the grinding wheel for CG and UVAG are observed, as shown in Fig. 6b and c. Continuous friction wear is most commonly found in CG. Plastic wear occurs on the abrasive grain when the tangential force of abrasive grain F_{gt} exceeds the yield strength of abrasive materials in the cutting process. This wear is gradual, and the grain is eventually worn flat. In addition, bond fracture and abrasive grain pull-out are observed when the shear force exceeds the bonding strength (Fig. 6b). Conversely, a random brittle fracture usually occurs in UVAG. Microcracks are generated because of the impact of contact between the WA grains and the workpiece material. The microfracture of grain is formed by removing small fragments from the sliding surface (Fig. 6c). These mechanical wear behaviours of the grinding wheel are related to the grinding times, effective contact length and grinding force. The impact times increase the abrasive grain, which is subjected to intermittent loads during UVAG, thereby effectively reducing the friction wear. Moreover, the self-sharpening of the grinding wheel is realised by increasing the microfracture of grains.

3.3 Chip topography

Chip formation is an important issue in controlling the grinding wheel performance or the machined surface in the grinding process. The metal chip shapes obtained by grinding are flowing, blocky, ripping, shearing and melting

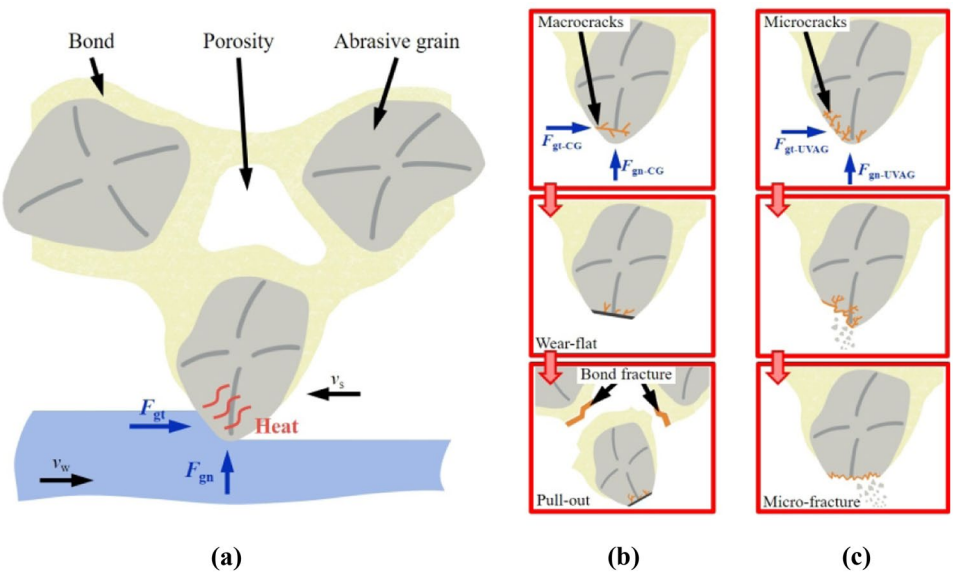

Fig. 6 Schematic of (**a**) force load and thermal load of a single abrasive grain and wear behaviours for CG (**b**) and UVAG (**c**)

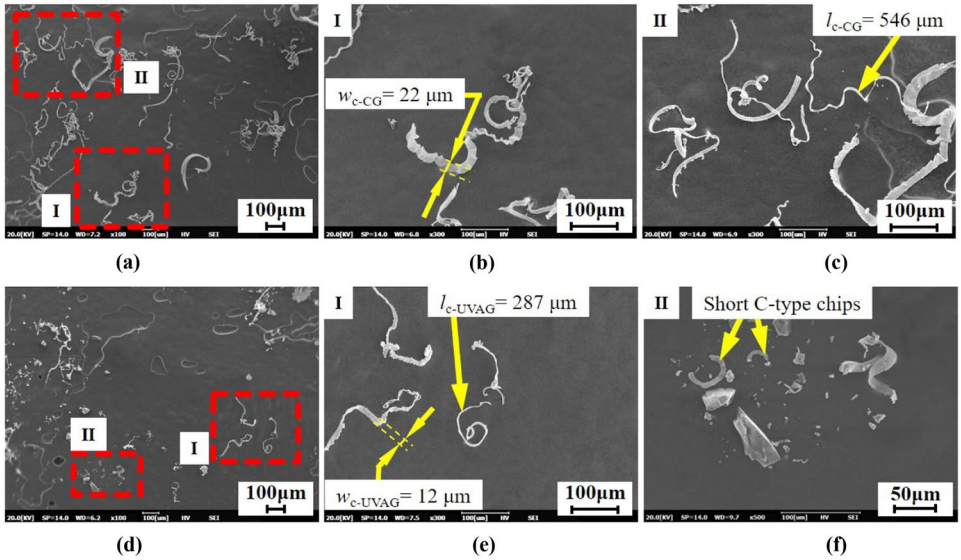

Fig. 7 SEM microstructures of chip morphologies. In (**a**), two enlarged views of the red dashed frames indicate the width (**b**) and length (**c**) of the chips under CG, and in (**d**), two enlarged views of the red dashed frames indicate the size of the chips (**e**) and C-type chips (**f**) under UVAG

chips [34]. Figure 7 shows the chip morphologies of CG and UVAG. Continuous chips are observed. The surface of the chips close to the rake face is smooth, whereas the surface away from the rake face is rough. As shown in Fig. 7a-c, for CG processes, the width of the chips ($w_{c\text{-}CG}$) in the measurement area I is 22 μm, and the length of the chips ($l_{c\text{-}CG}$) in the measurement area II is 546 μm. As shown in Fig. 7d-e, the width and length of the chips ($w_{c\text{-}UVAG}$ and $l_{c\text{-}UVAG}$) in the measurement area I for UVAG processes are 12 and 287 μm, respectively. Moreover, short C-type chips are generated in UVAG, as observed in area II shown in Fig. 7f.

The chip generation behaviours of CG and UVAG are schematically illustrated in Fig. 8. The continuous chips generally appear under the condition of small cutting depth and high grinding speed in the grinding of plastic metal materials. Compared with UVAG, CG exhibits a continuous and stable cutting path of abrasive grain. Moreover, the chips in CG are wider and longer than those in UVAG. By contrast, the cutting trajectory changes, and a separation stage between the abrasive grain and the workpiece exists. The corresponding continuous chips are broken into small chips with thin and short structures in UVAG. In a sense, the chip breaking is realised by the separation characteristic of UVAG.

3.4 Surface quality

The surface quality considerably affects the performance of the parts and the reliability of the machine. The measurement direction of surface roughness R_a is perpendicular to the grinding infeed direction. The effects of MRR on the R_a value in the UVAG process are revealed in Fig. 9a. The surface roughness

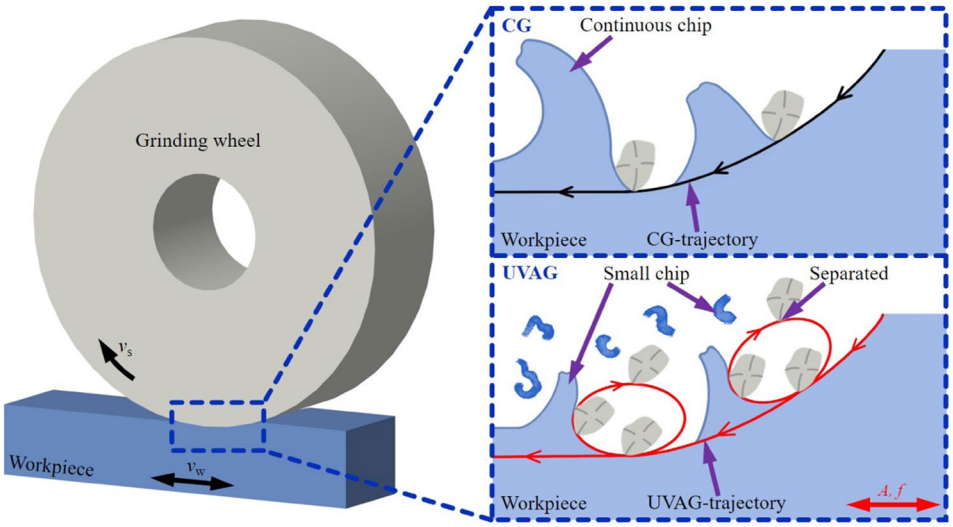

Fig. 8 Schematic of chip generation behaviours of CG and UVAG

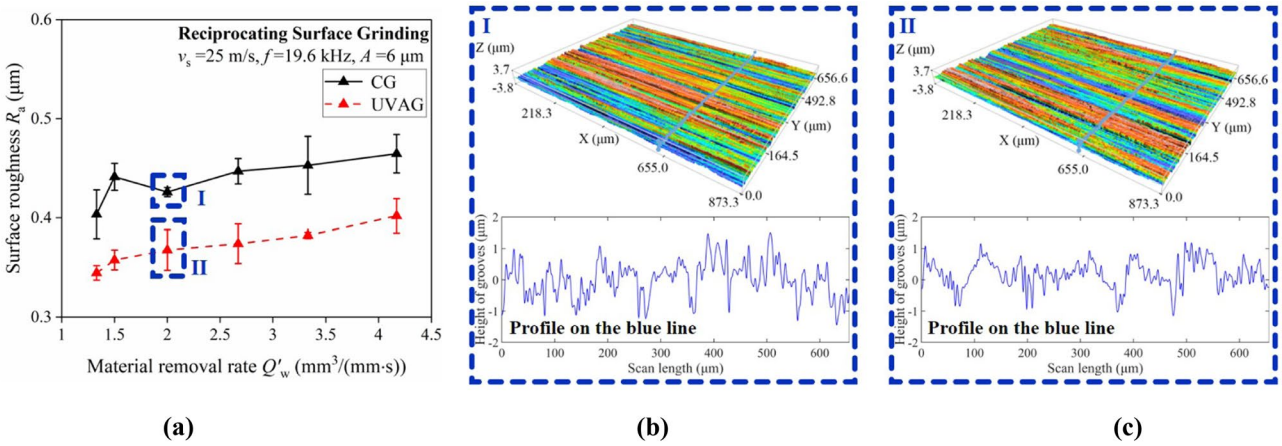

Fig. 9 Ground surface roughness versus MRR in CG and UVAG (**a**) and ground surface profile produced by CG (**b**) and UVAG (**c**) with $Q'_w = 2$ mm³/(mm·s)

values of two different grinding strategies have the same variation trend with the increased MRR. The R_a values are proportional to MRR. With the MRR increasing from 1.33 to 4.17 mm³/(mm·s) and grinding speed of $v_s = 25$ m/s, the R_a value of CG and UVAG increases from 0.4 to 0.46 μm and from 0.34 to 0.4 μm, respectively. The R_a value is reduced by up to 18.96% in UVAG. Figure 9b and c show the ground surface profiles obtained using the two types of grinding strategies in the case of $Q'_w = 2$ mm³/(mm·s). The peak-to-peak values for the height of grooves on the ground surface in CG and UVAG are from −1.440 to 1.504 μm and from −1.146 to 1.204 μm, respectively. The R_a value is related to the height of the residual area of the workpiece. The tangential residual height of the workpiece surface is reduced by repeatedly ironing the grinding wheel in UVAG. As a result, the grinding quality of UVAG is better than that of the other method [35].

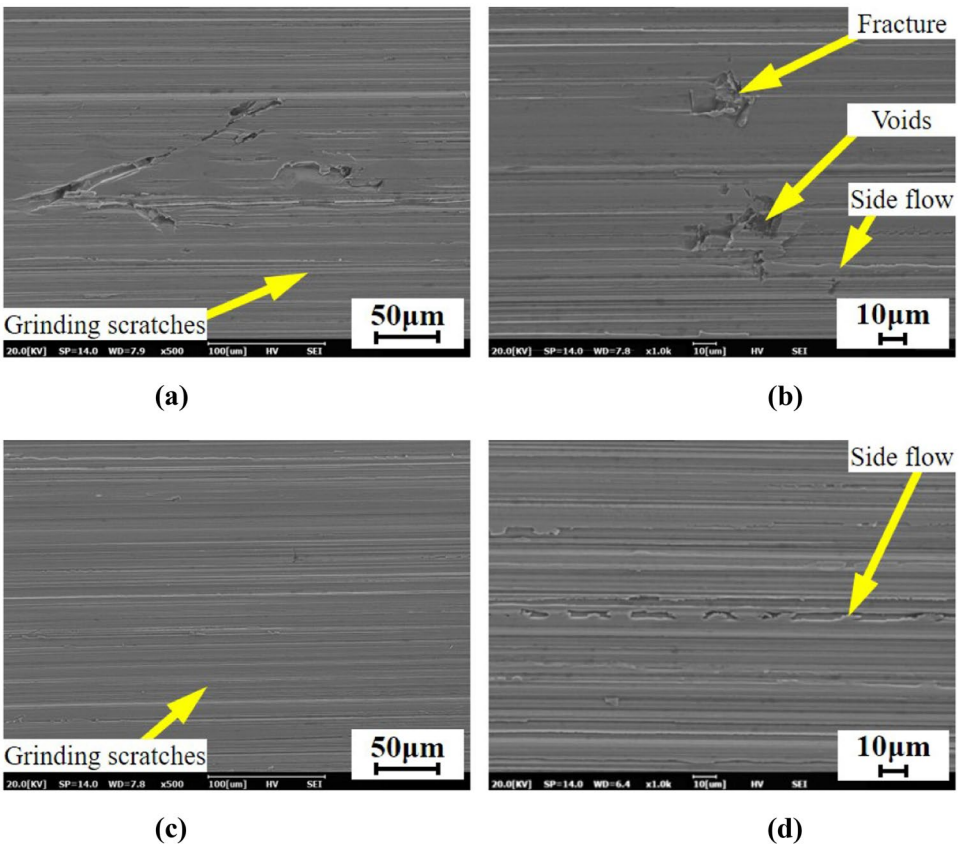

Fig. 10 Ground surface morphologies during CG (**a, b**) and UVAG (**c, d**) with $Q'_w = 2$ mm³/(mm·s)

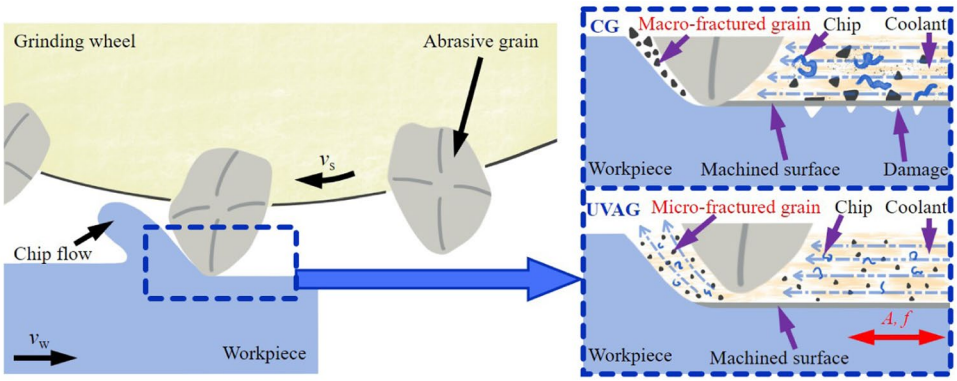

Fig. 11 Schematic of grinding surface generation for CG and UVAG

The SEM observation of the ground surface morphologies and surface damage during CG and UVAG is shown in Fig. 10. The ground surface quality of UVAG is better than that of CG when MRR is fixed at 2 $mm^3/(mm{\cdot}s)$. The various defect patterns with a large area on the machined surface are clearly observed in CG. They appear as irregular areas, material fractures, voids and redeposited material (Fig. 10a and b). Compared with that in CG, the machined surface in UVAG presents excellent surface textures except for some grinding marks because of the cutting trajectory of the abrasive grain (Fig. 10c and d).

The workpiece surface topography is the comprehensive effect of rubbing, ploughing and cutting abrasive grains on the workpiece. The material removal mechanism of a single abrasive was analysed because of the ground surface morphology characteristics of the workpiece. The abrasive grain is often considered a negative rake tool in the grinding process, and chips flow out from the rake face of abrasive grain. Figure 11 shows the forming mechanism of the ground surface. For CG, the abrasive grain continuously contacts the workpiece, and the heat on the rake face increases because the coolant cannot enter the rake face. The workpiece material easily adheres to the surface of the grinding wheel, and then redeposition occurs. In addition, the large-size wear debris mixed in the coolant is equivalent to free abrasive. This debris easily damages the ground surface as irregular area, fracture, void and other characteristics. For UVAG, the size of wear debris is small, and the coolant flow field is changed by the separation of grain and workpiece, which can take much heat and abrasive fragments away in time [36–38]. Therefore, the advantages of UVAG in intermittent grinding and reciprocating ironing can be used to reduce material damage. UVAG is also beneficial to surface integrity.

4 Conclusions

In this work, ultrasonic vibration was applied to the grinding of hardened GCr15 steel to demonstrate the advantages of composite processing. The grinding behaviour, including the grinding force and force ratio, wheel wear surface and chip topography, as well as ground surface quality, were discussed in detail. The following conclusions are obtained:

1. The material removal mechanism is changed by the separation characteristics of UVAG. Compared with CG, UVAG exhibits reduced grinding force, and a stable grinding force ratio is obtained. Moreover, the normal grinding force is steady at MRV of 135–315 mm^3 during the reciprocating surface grinding with ultrasonic vibration.
2. The grinding process is discontinued by the high-frequency action between abrasive grains and workpiece material in the UVAG process. The phenomenon of chip clogging and adhesion is reduced, and the wear patterns of abrasive grains exhibit microfracture, which can effectively increase the self-sharpening capability of the grinding wheel.
3. The chip sizes in CG and UVAG differ. Small chips with thin and short structures are observed in UVAG. In addition, the short C-type chips observed in the experiment also prove that chip breaking is effectively achieved by the separation characteristic of UVAG.
4. UVAG is beneficial to surface integrity. The surface roughness R_a is reduced with the feature of reciprocating ironing in UVAG. The coolant flow field changes with the intermittent nature of UVAG, which can remove chips and grinding thermal load in time, thereby reducing ground damage.

Author contribution Yutong Qiu: experimentation, data curation and writing the original draft. Biao Zhao: data collection and manuscript revision. Yang Cao: experimentation and methodology. Wenfeng Ding: supervision, conceptualisation and methodology. Yucan Fu: resources and funding acquisition.

Funding This work was financially supported by the National Natural Science Foundation of China (Nos. 51921003 and 52175415), Natural Science Foundation of Jiangsu Province (No. BK20210295), National Key Laboratory of Science and Technology on Helicopter

Transmission (Nanjing University of Aeronautics and Astronautics) (No. HTL-A-20G01) and the Foundation of Graduate Innovation Centre in NUAA (No. KFJJ20200506).

Availability of data and material All data generated or analysed during this study are included in the present article.

Declarations

Ethics approval and consent to participate The article follows the guidelines of the Committee on Publication Ethics (COPE) and involves no studies on human or animal subjects.

Consent to participate Not applicable.

Consent for publication Not applicable.

Competing interests The authors declare no competing interests.

References

1. Guo XZ, Shi ZY, Yu B, Zhao BY, Li K, Sun YQ (2020) 3D measurement of gears based on a line structured light sensor. Precis Eng 61:160–169. https://doi.org/10.1016/j.precisioneng.2019.10.013
2. Hu QC, Chen XB, Xu ZY, Mai QL, Zhu C (2020) Study on kinematic characteristics of planetary multistage face gears transmission. Proc Inst Mech Eng D J Automob Eng 234:572–585. https://doi.org/10.1177/0954407019855908
3. Waller MD, McIntyre SM, Koudela KL (2020) Composite materials for hybrid aerospace gears. J Am Helicopter Soc 65:1–11. https://doi.org/10.4050/JAHS.65.042010
4. Li Q, Xie LY, Song JX, Li HY, Xu GL (2019) Research methods and applications of gear manufacturing process optimization. Math Probl Eng 2019:1–17. https://doi.org/10.1155/2019/7043604
5. Guerrini G, Lerra F, Fortunato A (2019) The effect of radial infeed on surface integrity in dry generating gear grinding for industrial production of automotive transmission gears. J Manuf Process 45:234–241. https://doi.org/10.1016/j.jmapro.2019.07.006
6. Miao Q, Ding WF, Xu JH, Cao LJ, Wang HC, Yin Z, Dai CW, Kuang WJ (2021) Creep feed grinding induced gradient microstructures in the superficial layer of turbine blade root of single crystal nickel-based superalloy. Int J Extreme Manuf 3:045102. https://doi.org/10.1088/2631-7990/ac1e05
7. Argoud V, Morel F, Pessard E, Bellett D, Thibault S, Gourdin S (2019) Fatigue behaviour of gear teeth made of case hardened steel: from competing mechanisms to lifetime variability. Procedia Struct Integr 19:719–728. https://doi.org/10.1016/j.prostr.2019.12.078
8. Li W, Liu BS (2018) Experimental investigation on the effect of shot peening on contact fatigue strength for carburized and quenched gears. Int J Fatigue 106:103–113. https://doi.org/10.1016/j.ijfatigue.2017.09.015
9. Sales WF, Schoop J, da Silva LR, Machado ÁR, Jawahir IS (2020) A review of surface integrity in machining of hardened steels. J Manuf Process 58:136–162. https://doi.org/10.1016/j.jmapro.2020.07.040
10. Wang WX, Salvatore F, Rech J, Li JY (2018) Comprehensive investigation on mechanisms of dry belt grinding on AISI 52100 hardened steel. Tribol Int 121:310–320. https://doi.org/10.1016/j.triboint.2018.01.019
11. Gu SS, Yang CY, Fu YC, Ding WF, Huang DS (2014) Grinding force and specific energy in plunge grinding of 20CrMnTi with monolayer brazed CBN wheel. Mater Sci Forum 770:34–38. https://doi.org/10.4028/www.scientific.net/MSF.770.34
12. Wang JJ, Zhang JF, Feng PF, Guo P (2018) Experimental and theoretical investigation on critical cutting force in rotary ultrasonic drilling of brittle materials and composites. Int J Mech Sci 135:555–564. https://doi.org/10.1016/j.ijmecsci.2017.11.042
13. Cao Y, Zhu YJ, Ding WF, Qiu YT, Wang LF, Xu JH (2021) Vibration coupling effects and machining behavior of ultrasonic vibration plate device for creep-feed grinding of Inconel 718 nickel-based superalloy. Chin J Aeronaut 35(2):332–345. https://doi.org/10.1016/j.cja.2020.12.039
14. Zheng FF, Kang RK, Dong ZG, Guo J, Liu JT, Zhang JT (2018) A theoretical and experimental investigation on ultrasonic assisted grinding from the single-grain aspect. Int J Mech Sci 148:667–675. https://doi.org/10.1016/j.ijmecsci.2018.09.026
15. Yang ZC, Zhu LD, Zhang GX, Ni CB, Lin B (2020) Review of ultrasonic vibration-assisted machining in advanced materials. Int J Mach Tools Manuf 156:103594. https://doi.org/10.1016/j.ijmachtools.2020.103594
16. Shen JY, Dai B, Wu X, Li Y, Hu ZW (2019) Study on the material removal mechanism of glass in single diamond grain grinding with ultrasonic vibration assisted. lnt J Abras Technol 9:60–72. https://doi.org/10.1504/IJAT.2019.097984
17. Bhaduri D, Soo SL, Aspinwall DK, Novovic D, Bohr S, Harden P, Webster JA (2017) Ultrasonic assisted creep feed grinding of gamma titanium aluminide using conventional and superabrasive wheels. CIRP Ann 66:341–344. https://doi.org/10.1016/j.cirp.2017.04.085
18. Bhaduri D, Soo SL, Novovic D, Aspinwall DK, Harden P, Waterhouse C, Bohr S, Mathieson AC, Lucas M (2013) Ultrasonic assisted creep feed grinding of Inconel 718. Procedia CIRP 6:615–620. https://doi.org/10.1016/j.procir.2013.03.044
19. Yu TB, Guo XP, Wang ZH, Xu PF, Zhao J (2019) Effects of the ultrasonic vibration field on polishing process of nickel-based alloy Inconel718. J Mater Process Technol 273:116228. https://doi.org/10.1016/j.jmatprotec.2019.05.009
20. Nik MG, Movahhedy MR, Akbari J (2012) Ultrasonic-assisted grinding of Ti6Al4V alloy. Procedia CIRP 1:353–358. https://doi.org/10.1016/j.procir.2012.04.063
21. Wang QY, Liang ZQ, Wang XB, Bai SW, Yeo SH, Jia S (2020) Modelling and analysis of generation mechanism of micro-surface topography during elliptical ultrasonic assisted grinding. J Mater Process Technol 279:116585. https://doi.org/10.1016/j.jmatprotec.2019.116585
22. Zhu YJ, Ding WF, Rao ZW, Zhao ZC (2019) Self-sharpening ability of monolayer brazed polycrystalline CBN grinding wheel during high-speed grinding. Ceram Int 45:24078–24089. https://doi.org/10.1016/j.ceramint.2019.08.115
23. Naskar A, Choudhary A, Paul S (2020) Wear mechanism in high-speed superabrasive grinding of titanium alloy and its effect on surface integrity. Wear 462:203475. https://doi.org/10.1016/j.wear.2020.203475
24. Zhao B, Ding WF, Xiao GD, Zhao JS, Li Z (2021) Effects of open pores on grinding performance of porous metal-bonded aggregated cBN wheels during grinding Ti–6Al–4V alloys. Ceram Int 47(22):31311–31318. https://doi.org/10.1016/j.ceramint.2021.08.004
25. Li BK, Yin JF, Zhu YJ, Zhang X, Ding WF (2021) Grain wear evolution of cubic boron nitride abrasives during single grain grinding of powder metallurgy superalloy FGH96. Ceram Int 47:2508–2516. https://doi.org/10.1016/j.ceramint.2020.09.094
26. Xi XX, Ding WF, Fu YC, Xu JH (2018) Grindability evaluation and tool wear during grinding of Ti_2AlNb intermetallics. Int J

Adv Manuf Technol 94:1441–1450. https://doi.org/10.1007/s00170-017-1005-7
27. Madopothula U, Lakshmanan V, Nimmagadda RB (2017) Time dependent behavior of alumina grains manufactured by two different routes while grinding of AISI 52100 steels. Arch Civ Mech Eng 17:400–409. https://doi.org/10.1016/j.acme.2016.11.004
28. Yang LJ, Wang L, Liu Q, Tian XL (2018) Grinding performance of a new micro-crystalline corundum wheel when form-grinding automobile gears. Int J Adv Manuf Technol 96:857–870. https://doi.org/10.1007/s00170-017-1514-4
29. Yang ZC, Zhu LD, Ni CB, Ning JS (2019) Investigation of surface topography formation mechanism based on abrasive-workpiece contact rate model in tangential ultrasonic vibration-assisted CBN grinding of ZrO2 ceramics. Int J Mech Sci 155:66–82. https://doi.org/10.1016/j.ijmecsci.2019.02.031
30. Li HN, Yu TB, Wang ZX, Li DZ, Wang WS (2017) Detailed modeling of cutting forces in grinding process considering variable stages of grain-workpiece micro interactions. Int J Mech Sci 126:319–339. https://doi.org/10.1016/j.ijmecsci.2016.11.016
31. Yu TY, Asplund DT, Bastawros AF, Chandra A (2016) Performance and modeling of paired polishing process. Int J Mach Tools Manuf 109:49–57. https://doi.org/10.1016/j.ijmachtools.2016.07.003
32. Tawakoli T, Azarhoushang B (2008) Influence of ultrasonic vibrations on dry grinding of soft steel. Int J Mach Tools Manuf 48:1585–1591. https://doi.org/10.1016/j.ijmachtools.2008.05.010
33. Miao Q, Ding WF, Kuang WJ, Yang CY (2020) Comparison on grindability and surface integrity in creep feed grinding of GH4169 K403 DZ408 and DD6 nickel-based superalloys. J Manuf Process 49:175–186. https://doi.org/10.1016/j.jmapro.2019.11.027
34. Nadolny K, Kapłonek W (2016) The effect of wear phenomena of grinding wheels with sol-gel alumina on chip formation during internal cylindrical plunge grinding of 100Cr6 steel. Int J Adv Manuf Technol 87:501–517. https://doi.org/10.1007/s00170-016-8500-0
35. Isobe H, Hara K (2017) Visualization of fluctuations in internal stress distribution of workpiece during ultrasonic vibration-assisted cutting. Precis Eng 48:331–337. https://doi.org/10.1016/j.precisioneng.2017.01.003
36. Paknejad M, Abdullah A, Azarhoushang B (2017) Effects of high power ultrasonic vibration on temperature distribution of workpiece in dry creep feed up grinding. Ultrason Sonochem 39:392–402. https://doi.org/10.1016/j.ultsonch.2017.04.029
37. Zhao B, Guo XC, Bie WB, Chang BQ, Zhao CY (2020) Thermo-mechanical coupling effect on surface residual stress during ultrasonic vibration-assisted forming grinding gear. J Manuf Process 59:19–32. https://doi.org/10.1016/j.jmapro.2020.09.041
38. Madarkar R, Agarwal S, Attar P, Ghosh S, Rao PV (2018) Application of ultrasonic vibration assisted MQL in grinding of Ti-6Al-4V. Mater Manuf Process 33:1445–1452. https://doi.org/10.1080/10426914.2017.1415451